Boundary-Layer Meteorol (2007) 122:343–365
DOI 10.1007/s10546-006-9100-6

ORIGINAL PAPER

Water tank and numerical model studies of flow over steep smooth two-dimensional hills

J. B. R. Loureiro · D. V. Soares · J. L. A. Fontoura Rodrigues · F. T. Pinho · A. P. Silva Freire

Received: 28 June 2005 / Accepted: 20 May 2006 /
Published online: 5 August 2006
© Springer Science+Business Media B.V. 2006

Abstract The present work investigates the role of different treatments of the lower boundary condition on the numerical prediction of flows over two-dimensional, smooth, steep hills. Four different law of the wall formulations are tested when a large recirculating region is formed on the lee side of the hill. Numerical implementation of the near-wall functions was made through a finite elements code. The standard κ–ϵ model was used to close the averaged Navier–Stokes equations. Results are validated through original data obtained in a water tank. Measurements resorted to laser Doppler anemometry. The experiment provide detailed data for the characterization of the reverse flow in the region between the separation and the reattachment points, with emphasis on the near wall region. The experimental wall shear stress distribution is compared with the results provided by the different laws of the wall showing good agreement. The numerical predictions are shown to vary markedly between different formulations.

Keywords Hill · κ–ϵ model · Laser-Doppler anemometry · Law of the wall · Separation · Wall shear stress.

J. B. R. Loureiro (✉) · A. P. Silva Freire
Mechanical Engineering Program (COPPE/UFRJ),
Federal University of Rio de Janeiro,
C.P. 68503, 21945-970, Rio de Janeiro, Brazil
e-mail: jbrloureiro@gmail.com

D. V. Soares · J. L. A. Fontoura Rodrigues
Department of Mechanical Engineering, University of Brasilia,
70910-900, Brasilia, Brazil

F. T. Pinho
Centro de Estudos de Fenómenos de Transporte,
Faculdade de Engenharia da Universidade do Porto,
Rua Dr. Roberto Frias s/n, 4200-465, Porto, Portugal

F. T. Pinho
Universidade do Minho, Largo do Paço, 4704-553, Braga, Portugal

1 Introduction

Non-uniformities resulting from changes in the surface are ubiquitous in micrometeorology, particularly surface roughness and hills. Unfortunately, from a mathematical point of view, both conditions are difficult to treat analytically. This fact is much aggravated by the plain realization that the two conditions often occur simultaneously in nature.

In this work we discuss the second condition, flow over hills. By considering the flow over a homogeneous surface, we aim at analysing changes in surface properties provoked by changes in surface elevation alone. In particular, we discuss the role of different treatments of the lower boundary condition on the numerical prediction of flow properties. This is an aspect of the numerical modelling of flow over a hill that has always been known to be deficient. Here, four different law-of-the-wall formulations are applied to the steep hill problem: the classical logarithmic expression, and the formulations of Mellor (1966), of Nakayama and Koyama (1984) and of Cruz and Silva Freire (1998, 2002). As presented, these formulations were specially introduced for the prediction of flows subject to strong adverse pressure gradients; additionally, in their original form, they were developed to describe flows over an aerodynamically smooth surface. Thus, they resort to the canonical two-layered boundary-layer structure to describe the far upstream undisturbed flow so that the existence of a viscous layer scaled by ν/u_* is considered (ν = fluid kinematic viscosity, u_* = friction velocity).

New data from a water-channel experiment of separated, aerodynamically smooth, turbulent flow over a steep hill are presented herein with the particular purpose of validating the numerically simulated data. The experiments include local measurements of the mean and turbulent quantities of the flow, and were made using laser Doppler anemometry. The two-dimensional hill was constructed with a Witch of Agnesi shape having a maximum 18.6°slope. A flow visualization study, not presented here, was also performed.

The occurrence of flow separation downstream of steep hills adds much complexity to the problem. In fact, when hills become steep enough to form large downstream recirculation regions, not only the flow in the separated region changes, but significant changes occur in the whole flow field over the hill. Under such conditions, many of the classical theories based on perturbation techniques break down. Quantifying the onset and extent of separation is hence a necessary and fundamental step for the characterization of the velocity field.

Therefore, the prediction of turbulent flow over a steep hill naturally lends itself to the use of non-linear models. That has, indeed, been the general trend over the last 10 years. The natural increase in computer power, together with the development of a host of turbulence models, has witnessed a large increase on the number of non-linear numerical simulations of atmospheric flows. Typical numerical simulations have included two-equation eddy-viscosity turbulence models, algebraic Reynolds stress models, second-order closure models and large-eddy simulation. All simulations, however, irrespective of the type of closure scheme chosen, suffer with the specification of the boundary conditions at the wall.

A common approach, then, is to use the logarithmic law-of-the-wall formulation. Unfortunately, the mechanisms present in flow separation are poorly understood so that the classical logarithmic expressions normally used to describe the flow in the near-wall region do not find their counterpart near the separation point and in

the reverse flow region. This fact clearly poses severe difficulties for a numerical simulation of the flow field, since any selected turbulence model should be capable of well representing all turbulence features down to the wall.

The present work studies the effects that a two-dimensional, steep, smooth hill has on the properties of a neutrally stable boundary layer. The analysis makes a comparison between numerical and experimental results, having its focus on two main points: (i) to assess the applicability of the four previously mentioned wall functions for the description of the near-wall flow, and, (ii) to provide detailed experimental data for the characterization of the recirculating flow in the region between the separation and the reattachment points, with emphasis on the near-wall region.

2 Law-of-the-wall formulations

We introduce the different law-of-the-wall formulations that will be used in the implementation of the numerical simulations.

Since the main concern of this work is to carry out a numerical simulation of the flow over a steep hill, just the main parts of the original derivations will be presented here. We must warn the reader that some of the derivations are quite detailed, a recurring feature that has really prevented us from going into too much detail. Still, to ensure legibility of the paper, the most relevant equations will be presented here in full. For a complete account of the formulations, the reader is referred to the original references.

2.1 The logarithmic law-of-wall formulation for a smooth wall

For turbulent flows over a smooth wall, Prandtl (1925) considered the existence of a region adjacent to the wall in which the total shear stress is nearly constant. Bearing in mind that viscosity must play a role in finding local solutions, a simple scaling analysis furnishes u_* and ν/u_* as the two relevant scaling parameters.

The analysis may follow either from dimensional arguments or by mixing-length theory. Here, the second route is taken. Then, for the turbulent part of the wall region we may write

$$\frac{\partial \tau_t^+}{\partial z^+} = \frac{\partial}{\partial z^+}(-\overline{u'^+ w'^+}) = \frac{\partial}{\partial z^+}\left(\varkappa^2 z^{+2}\left(\frac{\partial u^+}{\partial z^+}\right)^2\right), \tag{1}$$

where the notation is standard. The dash denotes a quantity fluctuation, $u^+ = u/u_*$, $\tau_t^+ = \tau_t/(\rho u_*^2)$, $\tau_t = -\rho\overline{u'w'}$, $\overline{u'^+ w'^+} = \overline{u'w'}/u_*^2$ and $z^+ = z/(\nu/u_*)$.

Upon two successive integrations, we have

$$u^+ = \varkappa^{-1} \ln z^+ + A, \tag{2}$$

the classical law of the wall for a smooth surface ($\varkappa = 0.4$, $A = 5.0$) and zero-pressure gradient flows.

The action of an arbitrary pressure rise in the inner layer will distort the velocity profile until the pressure gradient is solely balanced by the gradient of shear stress. Near a separation point, Eq. (2) presents clear difficulties as $u_* \to 0$.

2.2 The law-of-the-wall formulation of Mellor (1966)

The effect of pressure gradients on the behaviour of turbulent boundary layers without restriction to equilibrium was investigated by Mellor (1966) through dimensional arguments. When a large external pressure gradient is applied to a boundary layer, no portion of the defect profile overlaps the logarithmic law. In fact, as previously suggested by Coles (1956) and by Stratford (1959), very near a separation point the logarithmic part of the velocity profile ceases to exist. However, if Millikan's (1939) arguments are recast and a new pressure gradient parameter is included in the analysis, an equation can be derived that satisfies the required limiting form as a separation point is approached.

Making the approximation that in the viscous sublayer the stress terms should be balanced only by the pressure term in the motion equations, Mellor (1966) found

$$u^+ = z^+ + \tfrac{1}{2}p^+ z^{+2}, \tag{3}$$

for the inner region of the boundary layer, whereas for the outer layer he wrote

$$u^+ = \xi_{p^+} + \frac{2}{\varkappa}\left(\sqrt{1+p^+z^+}-1\right) + \frac{1}{\varkappa}\ln\left(\frac{4z^+}{2+p^+z^+ + 2\sqrt{1+p^+z^+}}\right), \tag{4}$$

where $z^+ = zu_{pv}/\nu$, $u^+ = u/u_{pv}$, $u_{pv} = [(\nu/\rho)(\mathrm{d}p/\mathrm{d}x)]^{1/3}$ and $p^+ = [(\nu/\rho)(\mathrm{d}p/\mathrm{d}x)]/u_*^3$. Equation (4) follows different asymptotic behaviours in the limiting cases $p^+ \to 0$ or ∞, tending respectively to the classical logarithmic law or to Stratford's equation. Function ξ_{p^+} is a known parameter having been determined numerically for a range of p^+ values (Table 1).

Equations (3) and (4) were specified for the viscous and logarithmic regions, respectively. For numerical purposes, these regions were considered to intersect at $z^+ = 11.64$, which was considered to be the point of mathematical intersection of the viscous and logarithmic regions for the classical law of the wall. Regarding the law-of-the-wall formulations that take into account the effects of adverse pressure gradients, the mathematical intersection of the inner and logarithmic functions depends on the value of the dimensionless pressure p^+.

2.3 The law-of-the-wall formulation of Nakayama and Koyama (1984)

Nakayama and Koyama (1984) obtained a law of the wall for boundary layers subject to adverse pressure gradients by conducting a one-dimensional analysis on the turbulent kinetic energy equation with assumptions of local similarity. Considering the two possible limiting cases of a constant stress layer and of a zero wall-stress layer, the authors propose a turbulent kinetic energy equation that upon integration yields,

$$u^+ = \frac{1}{\varkappa^+}\left[3(\zeta - \zeta_s) + \ln\left(\frac{\zeta_s+1}{\zeta_s-1}\frac{\zeta-1}{\zeta+1}\right)\right], \tag{5}$$

Table 1 Integration function (Mellor, 1966), p^+

p^+	−0.01	0.00	0.02	0.05	0.1	0.2	0.5	1	2	10
ξ_{p+}	4.92	4.90	4.94	5.06	5.26	5.63	6.44	7.34	8.49	12.13

where

$$\zeta = \left(\frac{1+2\tau^+}{3}\right)^{1/2}. \tag{6}$$

The above formulation introduces a von Kármán modified constant, $\varkappa^+$, and the slip value, ζ_s. For a boundary layer subject to an adverse pressure gradient,

$$\tau^+ = 1 + p^+ z^+, \tag{7a}$$

$$p^+ = \nu\rho^{1/2}(\mathrm{d}\tau/\mathrm{d}z)_w/\tau_w^{3/2}, \tag{7b}$$

$$z^+ = (\tau_w/\rho)^{1/2} z/\nu. \tag{7c}$$

The von Kármán modified constant was estimated to be

$$\varkappa^+(p^+) = \frac{0.419 + 0.539p^+}{1+p^+}. \tag{8}$$

The slip value ζ_s was determined from the condition that in the limiting case $p^+ \to 0$ the above formulation reduces to the classical law of the wall, Eq. (2). It follows that

$$\zeta_s(p^+) = (1 + (2/3)\mathrm{e}^{-\varkappa A}p^+)^{1/2} \approx (1 + 0.074p^+)^{1/2}. \tag{9}$$

Nakayama and Koyama (1984) considered their analysis general in the sense that velocity was related to the local shear stress instead of to the distance from the wall. Additionally, the analysis does not have to be restricted to a linear velocity–stress relation but can be applied for any monotonically increasing shear stress layer.

2.4 The law-of-the-wall formulation of Cruz and Silva Freire (1998, 2002)

Introducing a new scaling procedure, Cruz and Silva Freire (2002) proposed the law of the wall for a separating flow to be written as

$$u = \frac{\tau_w}{|\tau_w|}\frac{2}{\varkappa}\sqrt{\frac{\tau_w}{\rho} + \frac{1}{\rho}\frac{\mathrm{d}P_w}{\mathrm{d}x}z} + \frac{\tau_w}{|\tau_w|}\frac{u_*}{\varkappa}\ln\left(\frac{z}{L_c}\right), \tag{10}$$

where

$$L_c = \frac{\sqrt{\left(\frac{\tau_w}{\rho}\right)^2 + 2\frac{\nu}{\rho}\frac{\mathrm{d}P_w}{\mathrm{d}x}u_R} - \frac{\tau_w}{\rho}}{\frac{1}{\rho}\frac{\mathrm{d}P_w}{\mathrm{d}x}}, \tag{11}$$

$\varkappa = 0.4$, u_* is the friction velocity, and u_R ($=\sqrt{\tau_p/\rho}$, τ_p = total shear stress) is a reference velocity.

The total shear stress, τ_p, can be evaluated from

$$\tau_p = C_\mu^{1/2}\rho\kappa_p + \mu\left|\frac{\partial u}{\partial z}\right|_p, \tag{12}$$

where the subscript p denotes an adequately chosen location, normally the first grid point in the computational domain, C_μ (= 0.09) is a constant of the κ–ϵ model and κ is the turbulent kinetic energy.

Equation (12) was obtained from a momentum balance in the near-wall region; it is similar to a relation usually employed by other authors to relate the wall shear stress to the turbulent kinetic energy in a κ–ϵ formulation (see, e.g., Launder and Spalding (1974), the only difference here is the inclusion of the viscous term to improve calculations when $z/L_c \leq 30$).

To find a first estimate for the wall shear stress, τ_{wo}, Eqs. (2) and (12) can be combined to give

$$\tau_{wo} = \frac{u_p C_\mu^{1/4} {\tau_p}^{1/2} \rho^{1/2} \varkappa}{\ln\left(E\, z\, \frac{(\tau_p/\rho)^{1/2}}{\nu}\right)}, \tag{13}$$

with $E = e^{\varkappa A}$.

The pressure gradient at the wall can be obtained through Eqs. (12) and (13),

$$\frac{\mathrm{d}P_w}{\mathrm{d}x} = \frac{\tau_p - \tau_{wo}}{z_p}, \tag{14}$$

which results directly from the inner layer approximated equations, and represents the balance of forces in that layer.

Next, the characteristic length can be calculated from

$$L_c = \frac{\sqrt{\left(\frac{\tau_{wo}}{\rho}\right)^2 + 2\frac{\nu}{\rho}\frac{\mathrm{d}P_w}{\mathrm{d}x}u_R} - \frac{\tau_{wo}}{\rho}}{\frac{1}{\rho}\frac{\mathrm{d}P_w}{\mathrm{d}x}}. \tag{15}$$

Finally, the wall shear stress is calculated from Eq. (10) according to

$$\tau_w = \frac{u_p {\tau_p}^{1/2} \rho^{1/2} \varkappa}{2\sqrt{\left|\frac{\tau_p}{\tau_{wo}}\right|} + \ln\left(\frac{z_p}{L_c}\right)}. \tag{16}$$

Using some production–dissipation equilibrium assumptions and Eq. (10) the kinetic energy dissipation and the production terms can be written respectively as follows:

$$\text{Dissipation} = {C_\mu}^{\frac{1}{2}} \kappa_p \left(\frac{(\tau_p/\rho)^{1/2}}{\varkappa z} + \frac{\frac{1}{\rho}\frac{dP_w}{dx}}{\varkappa (\tau_p/\rho)^{1/2}} \right), \tag{17}$$

$$\text{Production} = \frac{{C_\mu}^{\frac{1}{2}} \kappa_p \rho}{z} \left(\frac{2(\tau_p/\rho)^{\frac{1}{2}}}{\varkappa} + \frac{|\,(\tau_{wo}/\rho)\,|^{\frac{1}{2}}}{\varkappa} \ln\left(\frac{z}{L_c}\right) \right). \tag{18}$$

Equation (10) is a generalization of the classical law of the wall and replaces the three expressions advanced in Cruz and Silva Freire (1998—their Eqs. (25), (26), (27)). Equation (11) is an expression for the near-wall region characteristic length, which is assumed to be valid in the attached and in the reverse flow regions.

Far away from the separation point, where the wall shear stress is positive and $z(\mathrm{d}P_w/\mathrm{d}x) << \tau_w$, Eq. (10) reduces to the classical law of the wall, Eq. (2),

$$u = \frac{2}{\varkappa} u_* + \frac{u_*}{\varkappa} \ln\left(\frac{z}{L_c}\right), \tag{19a}$$

$$L_c = \nu/u_*. \tag{19b}$$

Near to the separation point where $\tau_w = 0$, Eq. (10) leads to

$$u = \frac{2}{\varkappa}\sqrt{\frac{z}{\rho}\frac{\mathrm{d}P_w}{\mathrm{d}x}}, \tag{20}$$

which is indeed Stratford's equation (see Stratford 1959).

In the reverse flow region where the wall shear stress is negative and $z(\mathrm{d}P_w/\mathrm{d}x) << \tau_w$, Eq. (10) reads

$$u = -\frac{2}{\varkappa}u_* - \frac{u_*}{\varkappa}\ln\left(\frac{z}{L_c}\right), \tag{21a}$$

$$L_c = 2\left|\frac{\tau_w}{\mathrm{d}P_w/\mathrm{d}x}\right|. \tag{21b}$$

The generalization provided by Eq.(10) implies that the friction velocity, u_*, used in the definition of L_c has to be replaced by the reference velocity u_R. Note that the characteristic length in the reverse flow region is different from the classical characteristic length given by the classical law of the wall. Equation (21) is in agreement with Simpson et al. (1981), who suggested that a characteristic length for the backflow region should be directly proportional to the absolute value of the wall shear stress.

3 Experiments

3.1 Description of the water channel and instrumentation

All experiments were carried out in a water channel sited at the Hydraulics Laboratory of the Civil Engineering Department, University of Oporto, Portugal. This water channel is an open-circuit, 17 m long channel with a cross-section of 0.4 m width and 0.6 m height. The water recirculation system consists of two underground tanks, four pumps with a maximum capacity of $150\,\mathrm{l\,s^{-1}}$ and one upper stabilizing tank. The working section was 3 m long, and was situated 7.3 m downstream of the channel entrance. The side walls were made of glass, so as to make it convenient to perform any visual inspection of the flow, as well as to permit an appropriate use of the laser Doppler anemometer (LDA). The model of the hill was located 8 m from the channel entrance.

During a typical experiment, two pumps sufficed to keep the system running in a steady state, with a maximum flow rate variation of $\pm 0.8\%$. At the entrance of the channel, the water was made to pass through a series of screens and filters so as to stabilize, make uniform and suppress any excessive level of turbulence. Screens and filters were also used to control the grain size of the particles in suspension in the water. To guarantee an accurate flow rate control, a magnetic flowmeter was installed in the supply line. The water depth along the channel was controlled by a vertical steel gate. The traversing system was 3D, very sturdy, independent of the water channel, and had a positioning precision of 10μm.

A one component, fibre optic, Dantec laser Doppler anemometry system was used in the forward scatter mode to measure the mean and the fluctuating velocity fields. The laser was a 2 W Ar-ion source operating in multi-mode. A Bragg cell unit was used

to introduce an electronic shift of 0.6 MHz. This procedure allowed for the resolution of the direction of the flow field and the correct measurement of near-zero mean velocities. Front lenses of 310 mm focal length were mounted on the probe in order to accurately position the measurement volume on the centreline of the channel. Before being collected by the photomultiplier, the scattered light passed through an interference filter of 514.5 nm, so that only green light was acquired. The signal from the photomultiplier was band-pass filtered and processed by a TSI 1990C counter, operating in single measurement per burst mode. A series of LDA biases were avoided by adjusting the strictest parameters on the data processor. For each point measured, a sample size of 10,000 values has been considered. Mean and root-mean-square (rms) values of fluctuating quantities have been defined over this sample size according to the Reynolds decomposition, which states that the instantaneous velocity equals the sum of a time-average component with a fluctuating component. The 10,000 sample size was observed to be sufficient to ensure independent velocity results at each point measured. Table 2 lists the main characteristics of the laser Doppler system used.

This system was used to measure both the longitudinal and the vertical velocity components. This was easily made by simply turning the probe around its axis, so that, for both conditions, the fringe distribution was perpendicular to the measured velocity component. As for the Reynolds shear stresses, measurements were made by turning the probe to the positions ±45°. For the undisturbed flow region, the uncertainties in the mean velocity components u and w are lower than 0.2% of the free stream velocity, u_δ. Further downstream of the hilltop, in high level turbulence regions, these maximum uncertainties increase to about 0.3% of the free stream velocity. As for the fluctuating quantities, $\sqrt{\overline{u'^2}}$, $\sqrt{\overline{w'^2}}$, and $\overline{u'w'}$, the estimated uncertainties in the undisturbed flow region are of 2.3%, 1.8%, 4.2% of the friction velocity in the undisturbed flow (for the Reynolds shear stress the uncertainty is given as a percentage of the square of the friction velocity of the undisturbed flow), respectively, increasing to 3.8%, 3.5% and 6.9% in regions of high turbulence.

3.2 Model hill characteristics

The model used in the present work was two-dimensional, axisymmetric and aerodynamically smooth. Based on the works of Britter et al. (1981) and of Arya et al. (1987), the shape of the hill followed a modified "Witch of Agnesi" profile, according to the equation $z_H = H_1[1 + (x/L_H)^2]^{-1} - H_2$. Thus, it follows that H $(= H_1 - H_2)$ $(= 60\,\text{mm})$ is the hill height and L_H $(= 150\,\text{mm})$ is the characteristic length of the hill representing the distance from the crest to the half-height point. Co-ordinates x and z represent the longitudinal and the vertical axes, respectively.

Table 2 Main characteristics of the laser Doppler system

Wavelength	514.5 nm
Half-angle between beams	3.415°
Fringe spacing	4.3183 μm
Frequency shift	0.60 MHz
Dimensions of the measurement volume	
Major axis	1.53 mm
Minor axis	162.0 μm

Table 3 Hill features

Characteristic height	H_1	75 mm
Characteristic height	H_2	15 mm
Hill height	H	60 mm
Hill length	L	600 mm
Distance from the crest to the half-height point	L_H	150 mm
Aspect ratio	$2L_H/H$	5
Maximum slope	$\theta_{\max}$	18.6°

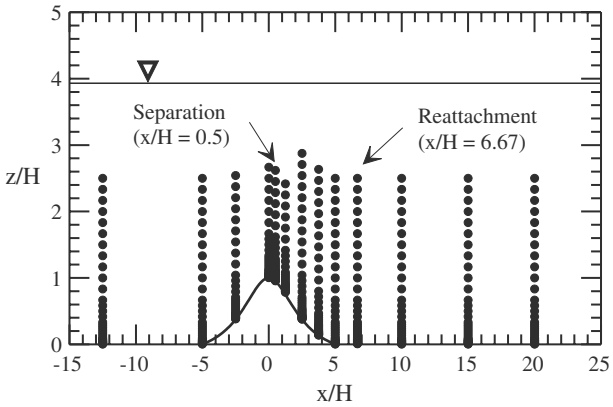

Fig. 1 Position of measuring stations and co-ordinate system

The geometry of the model was chosen so as to simulate a steep hill with a large recirculation region, and the model was made of a single sheet of polished plexiglass. The characteristic parameters of hill are presented in Table 3.

When the hill was not in place, mean velocity results obtained in the x–z planes (see Fig. 1) located 50 mm away from the channel centreline to the right and to the left showed a variation of 2% in relation to measurements taken at the channel centreline. When the hill was in place, this value showed a variation of about 3%.

3.3 Experimental results

Results will be presented for the 13 stations indicated in Fig. 1 with the main purpose of serving as validation data for the numerical calculations to be introduced next. To that end, we will strive in furnishing mean velocity data. However, and since a detailed investigation of the turbulent properties was performed, some turbulent results will also be presented. Please note the position of the co-ordinate system origin. Presentation of the data are split into three blocks: data for the flow field upstream of the separation point (first three stations), data for the re-circulation region (next seven stations) and data for the returning to equilibrium region (last three stations).

Results are mainly presented as plots with linear axes, as is normally the case. However, since in the comments below some mention will be made of the logarithmic behaviour of the velocity field, four representative profiles are shown in log-linear coordinates (Fig. 2d) so as to illustrate the referred behaviour.

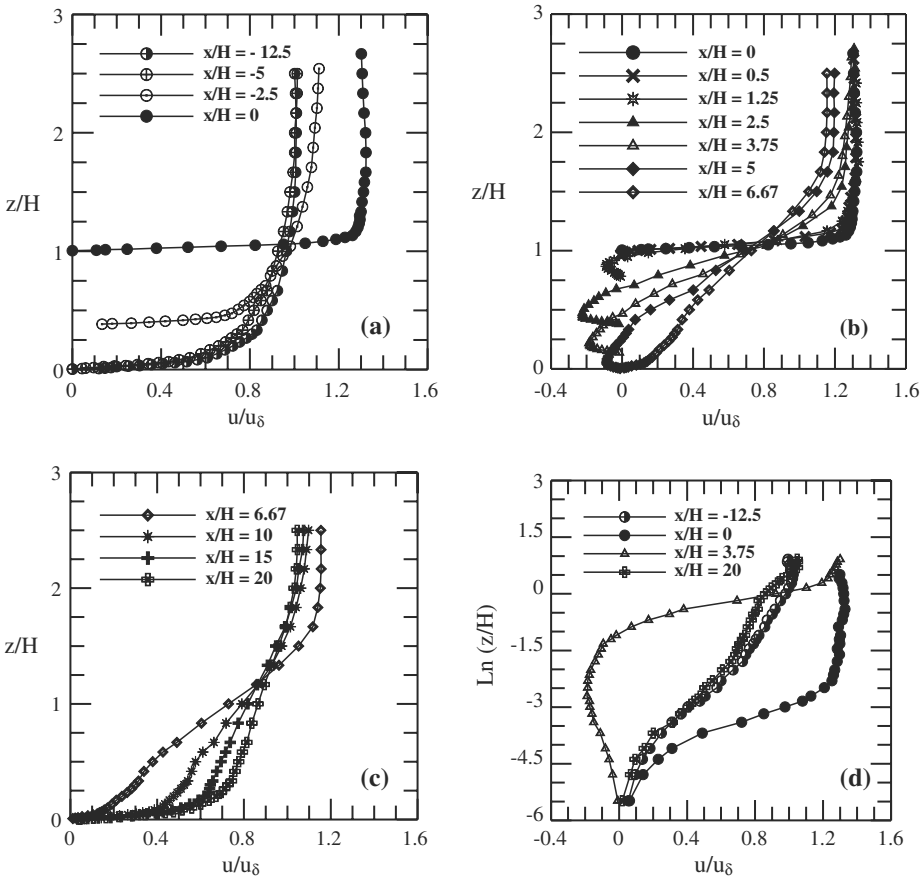

Fig. 2 Mean velocity profiles, x-component (**a–c**). Four representative logarithmic profiles are shown in (**d**)

Figures 2 and 3 show the mean velocity profiles. The flow acceleration region on the upstream side of hill is illustrated in Fig. 2a, and at stations $x/H = -12.5, -5$ and -2.5 the well-known law of the wall is very well discriminated. Figure 2d illustrates the logarithmic velocity profile measured at $x/H = -12.5$. In all three profiles, at least 11 points could be identified as belonging to the logarithmic region, yielding straight lines with coefficients of determination R^2 higher than 0.99. In addition, seven extra points were observed to be located in the viscous region; von Kármán's constant was found to be 0.39.

The local properties of the boundary layer in the undisturbed flow are shown in Table 4. The longitudinal and vertical fluctuations obtained in this experiments are representative of atmospheric values. This fact can be inferred from a comparison with typical values of near-surface fluctuations in neutrally stratified flows. For example, the following data are taken from the literature: $\sqrt{\overline{u'^2}}/u_* = 2.3$ and $\sqrt{\overline{w'^2}}/u_* = 1.1$ (Grant 1992), $\sqrt{\overline{u'^2}}/u_* = 2.12$ (Britter et al. 1981), $\sqrt{\overline{u'^2}}/u_* = 2.5$ and $\sqrt{\overline{w'^2}}/u_* = 1.2$ (Khurshudyan et al. 1981), $\sqrt{\overline{u'^2}}/u_* = 2.2$ and $\sqrt{\overline{w'^2}}/u_* = 1.0$ (Gong and Ibbetson 1986) and $\sqrt{\overline{u'^2}}/u_* = 2.19$ and $\sqrt{\overline{w'^2}}/u_* = 1.12$ (Athanassiadou and Castro 2001).

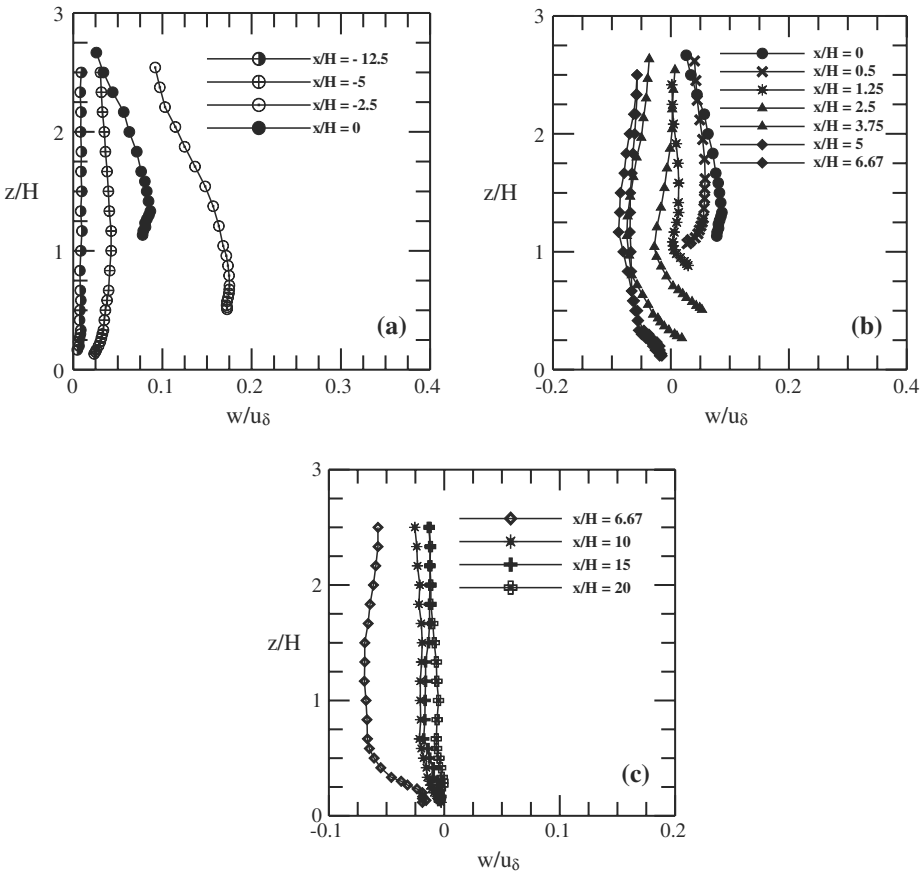

Fig. 3 Mean velocity profiles, z-component

Table 4 Properties of undisturbed profile

Boundary layer thickness	δ	100 mm
External velocity	u_δ	0.0482 m s^{-1}
Friction velocity	u_*	0.0035 m s^{-1}
Roughness length	z_0	0.27 mm
Longitudinal velocity fluctuations ($z/\delta = 0.05$)	$\sqrt{\overline{u'^2}}/u_*$	2.50
Transversal velocity fluctuations ($z/\delta = 0.08$)	$\sqrt{\overline{w'^2}}/u_*$	0.83

The reverse mean flow region is shown in Fig. 2b. In this flow region, no clear logarithmic region, as expected from the classical law of the wall, could be identified (stations $x/H = 0$ and $x/H = 3.75$ are illustrated in Fig. 2d). However, the viscous region could be discriminated for each profile from, at least, eight near-wall points. The separation region was observed to have a total length of about 370 mm ($= 6.17\,H$), as characterized by the curve defined by the points where the mean flow velocity is zero (Fig. 4). An outline of the region of trapped recirculating flow, here called the border of the recirculation region, is also shown in Fig. 4.

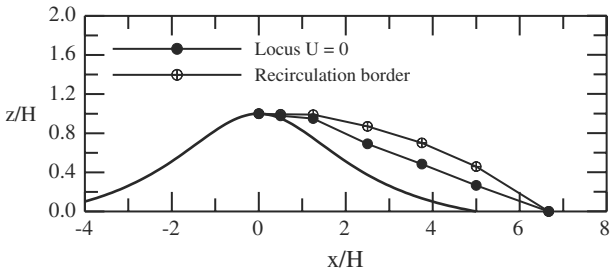

Fig. 4 Locus of zero longitudinal velocity in the re-circulation region

The mean longitudinal velocity profiles downstream of the hill are presented in Fig. 2c. Although much disturbed by the separation region, all four quoted profiles presented well-discriminated logarithmic regions. In fact, at least 12 points were used to determine the logarithmic region through straight lines with coefficients of determination, R^2, higher than 0.99 (station $x/H = 20$ is shown in Fig. 2d).

The mean z-velocity profiles, w, show a large increase as the fluid flows uphill (Fig. 3a), followed by negative values of velocity on the downside of the hill (Fig. 3b). In fact, due to the extension of the separation bubble that is formed, the mean z-velocity profile only becomes negative past station $x/H = 2.5$. As station $x/H = 10$ is reached (Fig. 3c), w returns to a near-zero value.

The changes in Reynolds stresses are shown in Figs. 5–7, where measurements indicate a decrease in $\overline{u'^2}$ on the upstream side of the hill, possibly due to the accelerated mean flow (Fig. 5a). In particular, on the hill top, a slight decrease in $\overline{u'^2}$ is observed. In the separated flow region (Fig. 5b), a substantial enhancement in $\overline{u'^2}$, of the order of four times, occurs. The large increase in $\overline{u'^2}$ results from the large turbulence production provoked by $P_{uu} = -2\overline{u'w'}(\partial u/\partial z)$. The peak value for $\overline{u'^2}$ was found for $x/H = 3.75$ and $z/H = 0.8$, near the centre of the recirculation bubble. In the flow separated region, the turbulence profiles are characterized by a maximum peak progressively moving away from the wall with increasing distance from the hill. Far away from the hill, at stations $x/H = 15$ and 20, the two $\overline{u'^2}$ profiles are still easily distinguished from each other and different from the undisturbed profile at $x/H = -12.5$.

For $\overline{w'^2}$ an increase of about 50% is observed at the hilltop as compared to the undisturbed values. This increase is followed by a further, and much more substantial, increase of about twentyfold in the separated flow region. Indeed, we had seen previously that a large increase in w was observed uphill. The role of this increase is, in its turn, to increase the production of $\overline{w'^2}$ through $P_{ww} = -2\overline{u'w'}(\partial w/\partial x)$.

The distributions of $\overline{u'^2}$ and of $\overline{w'^2}$ are somewhat similar across the separated region, although $\overline{w'^2}$ is about 65% of $\overline{u'^2}$. Indeed, the turbulence production $P_{uu} = -2\overline{u'w'}(\partial u/\partial z)$ is expected to exceed the term $P_{ww} = -2\overline{u'w'}(\partial w/\partial x)$, since in this region $(\partial u/\partial z) > (\partial w/\partial x)$. Also, we note that the maximum value of $\overline{w'^2}$ is found at $x/H = 3.75$, $z/H = 0.8$, just as before. Far away from the hill, at stations $x/H = 15$ and 20, the two $\overline{w'^2}$ profiles are still very different from each other.

The Reynolds stress profile, $-\overline{u'w'}$, is relatively small upwind of the hill and varies slowly with height. At the hill crest, values of $-\overline{u'w'}$ are enhanced. In the shear layer

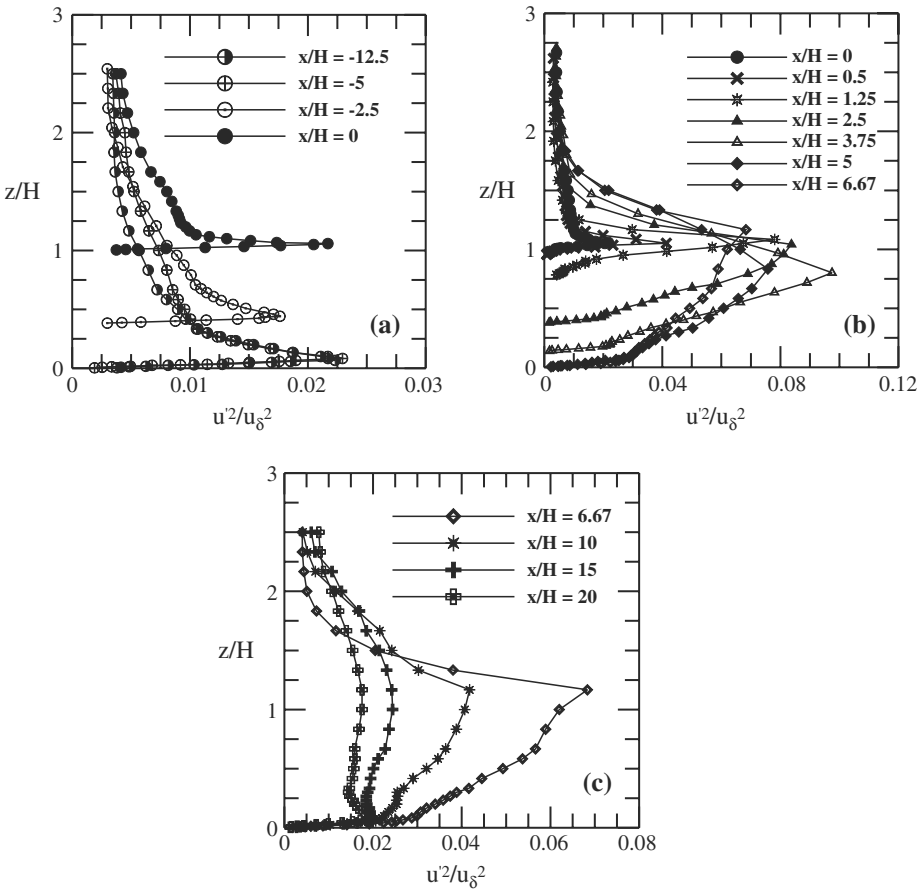

Fig. 5 Normalized Reynolds stress profiles, $\overline{u'^2}/u_\delta^2$

that is formed at the top of the flow separated region, a large increase in $-\overline{u'w'}$ is observed, of the order of 17 times. This is due to the enhanced shear effects through the production term $P_{uw}=-2\overline{w'^2}(\partial u/\partial z)$. The highest value of $-\overline{u'w'}$ is achieved at location $x/H = 3.75$, $z/H = 0.6$, differently from the positions of the points of maximum for $\overline{u'^2}$ and for $\overline{w'^2}$. Between the locations of detachment and of re-attachment, an inner region of constant $-\overline{u'w'}$ was not detected. Far downstream of the hill, at stations $x/H = 15$ and 20, $-\overline{u'w'}$ becomes nearly constant.

To find the wall shear stress in regions where the flow is attached chart methods based on the logarithmic law may be used under some conditions. Additionally, the identification of an existing constant shear-stress wall layer can also be used. In a reverse flow region, however, some alternative technique has to be used to find the wall shear stress.

Consider that in a turbulent boundary layer the very near-wall region is dominated by viscous effects. Then, under adverse pressure gradient conditions, the momentum equation in the viscous sublayer has approximate balance of the viscous and pressure terms. A double integration of this equation furnishes a second-degree polynomial

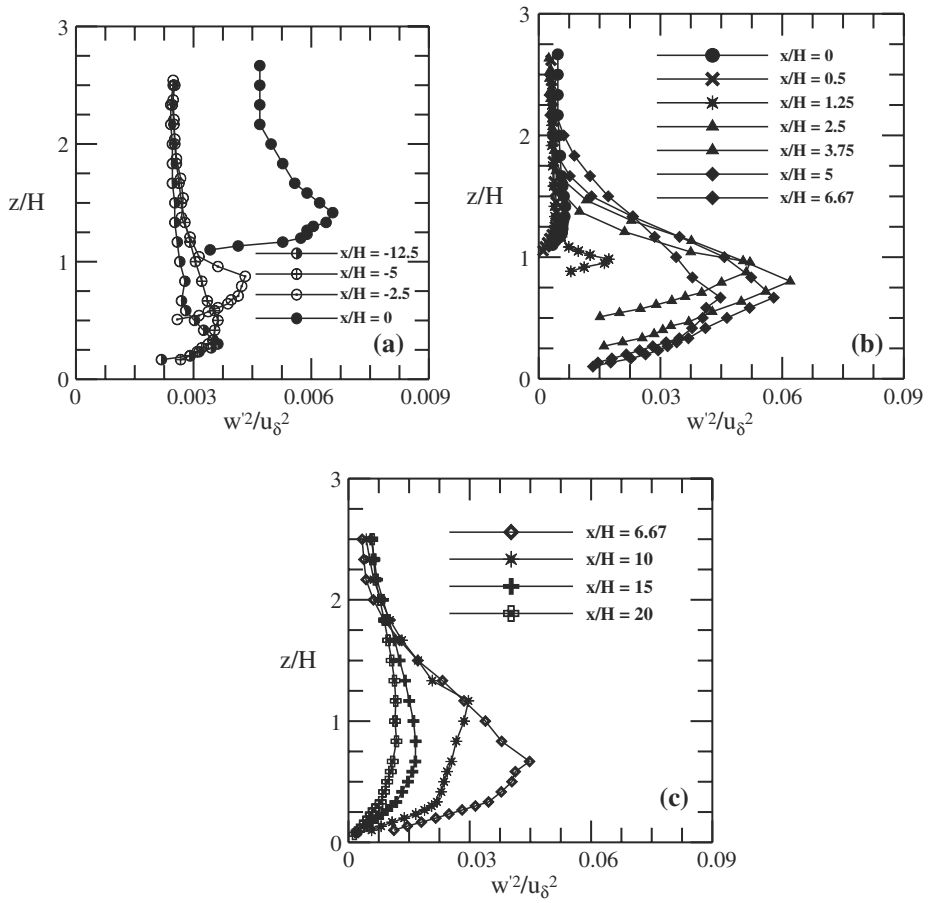

Fig. 6 Normalized Reynolds stress profiles, $\overline{w'^2}/u_\delta^2$

relationship between the velocity and the distance from the wall, as shown previously in non-dimensional form by Eq. (3). In dimensional form, Eq. (3) reads

$$u = \frac{1}{2\mu}\frac{\partial p}{\partial x} z^2 + \frac{\tau_w}{\mu} z. \tag{22}$$

The correct application of the above equation to the experimental data requires the specification of an adequate coordinate system. For flows over a flat wall, the x-coordinate can be aligned with the mean flow direction, resulting in a rectangular Cartesian system where the momentum balance in the x-direction contains most of the dynamical information regarding the flow. For flows over curved surfaces, Finnigan (1983) suggests the use of physical streamlined coordinates. These coordinates are, however, difficult to use in separated flow regions.

Here, at least eight measurement points were located in the first 3 mm away from the wall. In our worst case scenario, the wall tangent corresponds to an angle of about 14° (station $x/H = 1.25$). Since $\sin(14°) = 0.24$, the corresponding streamwise velocity displacement along the normal direction will occur over a maximum distance

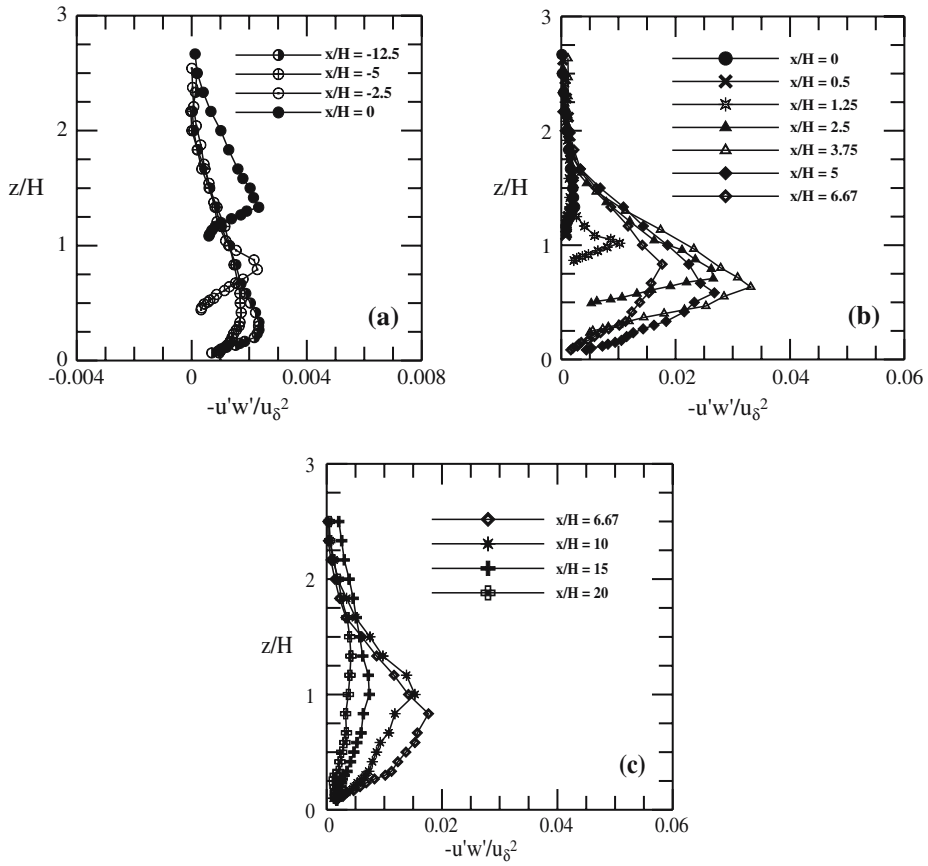

Fig. 7 Normalized Reynolds stress profiles, $-\overline{u'w'}/u_\delta^2$.

of 0.7 mm. This fact, allied to the fact that $u >> w$, means that close to the surface the wall shear stress can be calculated directly from Eq. (22) with the rectangular Cartesian system shown in Fig. 1.

4 Numerical simulation

4.1 Computational details

The numerical simulations were performed with the code Turbo-2D (Fontoura Rodrigues 1990), which is a two-dimensional code based on the finite element method. The application of standard Galerkin discretization to problems that are dominated by convection, frequently leads to non-physical oscillations and convergence difficulties. To alleviate this tendency, code Turbo-2D resorts to the balance dissipation method proposed by Hughes and Brooks (1979) and Kelly et al. (1980) and implemented by Brun (1988). The structure of code Turbo-2D was based on the work of Brison et al. (1985), which uses finite elements of type P1-isoP2 for space discretization and a semi-implicit time discretization.

The governing equations are the Reynolds averaged equations for an incompressible flow. Using the repeated indices convention, these equations can be written in non-dimensional form as

$$\frac{\partial u_i}{\partial x_i} = 0, \tag{23}$$

$$\frac{\partial u_i}{\partial t} + \frac{\partial}{\partial x_j}(u_i u_j) = -\frac{\partial p}{\partial x_i} + \frac{1}{R_\mathrm{e}}\frac{\partial}{\partial x_j}\left(\frac{\partial u_i}{\partial x_j} + \frac{\partial u_j}{\partial x_i}\right) - \frac{\partial}{\partial x_j}\left(\overline{u_i' u_j'}\right), \tag{24}$$

where u_i represents the normalized velocity components, p the normalized pressure and R_e the Reynolds number.

The Reynolds equations are complemented by the eddy viscosity formulation

$$-\overline{u_i' u_j'} = \nu_t\left(\frac{\partial u_i}{\partial x_j} + \frac{\partial u_j}{\partial x_i}\right) - \frac{2}{3}\kappa\delta_{ij}, \tag{25}$$

where ν_t denotes the eddy viscosity and δ_{ij} is the Kronecker delta.

In Eq. (25), κ is the turbulent kinetic energy,

$$\kappa = \tfrac{1}{2}\overline{u_i' u_i'}. \tag{26}$$

In the κ–ϵ model, the eddy viscosity is taken to be

$$\nu_t = C_\mu \frac{\kappa^2}{\varepsilon}, \tag{27}$$

where, $C_\mu (= 0.09)$ is a constant of the κ–ϵ model, and ε is the dissipation rate of κ.

Equations for κ and for ε can be obtained directly from the Reynolds equations through some algebraic manipulations. With further modelling, the resulting equations can be cast as

$$\frac{\partial \kappa}{\partial t} + u_i\frac{\partial \kappa}{\partial x_i} = \frac{\partial}{\partial x_i}\left[\left(\frac{1}{R_\mathrm{e}} + \left(\frac{1}{R_\mathrm{t}\sigma_\kappa}\right)\right)\frac{\partial \kappa}{\partial x_i}\right] + P_{u_i u_j} - \varepsilon, \tag{28}$$

$$\frac{\partial \varepsilon}{\partial t} + u_i\frac{\partial \varepsilon}{\partial x_i} = \frac{\partial}{\partial x_i}\left[\left(\frac{1}{R_\mathrm{e}} + \left(\frac{1}{R_\mathrm{t}\sigma_\varepsilon}\right)\right)\frac{\partial \varepsilon}{\partial x_i}\right] + C_{\varepsilon 1}\frac{\varepsilon}{\kappa}P_{u_i u_j} - C_{\varepsilon 2}\frac{\varepsilon^2}{\kappa}, \tag{29}$$

where R_t is the turbulent Reynolds number defined with the help of Eq. (27).

Constants $C_\mu, C_{\varepsilon 1}, C_{\varepsilon 2}, \sigma_k$ and σ_ε, as given in the literature, take values: 0.09, 1.44, 1.92, 1.0, 1.3. The production term, $P_{u_i u_j}$, is given by

$$P_{u_i u_j} = -\overline{u_i' u_j'}\frac{\partial u_j}{\partial x_i}. \tag{30}$$

The governing equations are discretized in space through triangular finite elements, defined by linear interpolation functions. The compatibility conditions between pressure and velocity fields are preserved by using two calculation meshes. The pressure field is calculated with a mesh with P1-type elements. Velocity and all other variables are calculated using a P1-isoP2 mesh, constructed from the P1 mesh by dividing one segment into two. This procedure generates four P1-isoP2 elements from one P1 element. Figure 8 shows the velocity and pressure meshes used to evaluate the flow field studied in this work.

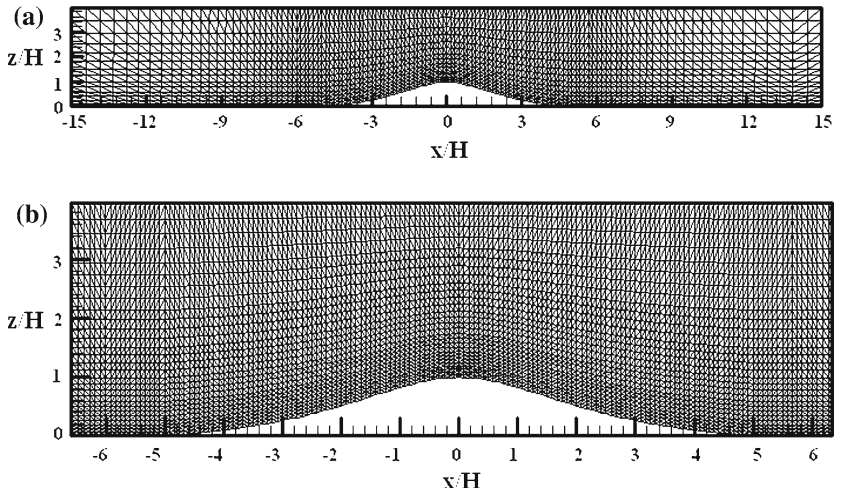

Fig. 8 Typical mesh distribution around the hill for pressure and velocity fields evaluation. (**a**) P1 mesh with 1875 nodes and 3472 elements. (**b**) Iso/P2 mesh with 7221 nodes and 13888 elements

Table 5 Comparative computational times required to achieve numerical convergence for each of the law of the wall formulation considered

Formulation	LogLaw	M (1966)	NK (1984)	CSF (1998)
Time	1	20	25	25

Temporal discretization of the governing equations is made through a sequential semi-implicit finite difference algorithm of Brison et al. (1985). The time iteration process was used to remove the influence of the initial conditions on the final calculations, so that simulation finishes only when statistically steady results have been reached. In fact, to keep a low sensitivity of the results to the time intervals, very fine timesteps would have to be used. Here, in order to optimize the convergence process, a temporal integration procedure that progressively increased the timesteps was used. In a typical simulation, initial timesteps were about 10^{-6} s. This value was then increased steadily to 5×10^{-2} s by the end of the simulation. These values were observed to ensure independence of results. For the velocity and pressure fields, and for the velocity boundary conditions, the convergence criteria were set respectively to 10^{-8} and 10^{-6}. Because computational (cpu) times vary with local parameters (processor features, memory capacity, grid refinement, convergence criteria), just comparative computational flow times are shown here (Table 5).

For code verification, Turbo-2D was tested against a number of data including the numerical solution of Mansour et al. (1989) and the experimental data for flows over a backward facing step and in an asymmetric plane diffuser (Carlson et al. 1967; Reneau et al. 1967; Kim et al. 1980; Trupp et al. 1986; Buice and Eaton 1995).

A successful simulation of the flow under scrutiny depends, of course, on the correct specification of the boundary conditions. Here, the inflow values of the mean velocity, of the turbulence kinetic energy and of the dissipation rate were taken directly from the experimental data. In the region adjacent to the surface, wall functions were used as explained next. At the top, a free surface condition was used. For the outflow, symmetry (zero normal gradient) conditions were applied.

Since the standard κ–ε turbulence model does not hold for low values of the turbulent Reynolds number, a common practice is to use wall functions to express the flow behaviour in the near-wall region, much as described in Sect. 3. In finite elements, the mesh does not reach the wall. Thus, the velocity tangent to the solid wall has to be specified as a function of the distance from the wall, d.

Clearly, the chosen value of d where the boundary conditions are to be applied must be selected so that $d^+ (= du_*/\nu)$ lies within the range of validity of the law of the wall. Thus, a posteriori computations of d^+ have to be performed. In many cases, computational decisions and meshing procedures do have an impact on the accuracy of numerical predictions. For most finite element codes, acceptable values of d^+ obey the relation $d^+ < 100$ in order to prevent numerical instabilities. For attached flows, the best results are normally found for $30 < d^+ < 50$. In the present algorithm, d is given as an initial value, and computations are usually started with small values of d. This value is then progressively increased until a maximum converged value is obtained. Ideally, the selected value of d should satisfy $30 < d^+$. This condition, however, normally can only be satisfied for attached flows. The ideal d is, in any case, always determined by trial-and-error.

During calculations, u and u_* at a given iteration are found through a system of non-linear equations. The explicit treatment of this non-linearity causes heavy numerical instabilities, independently of the type of law of the wall that is adopted. Thus, the introduction of a stabilization scheme for the calculation of u_* by a sub-relaxation method is in order. Turbo-2D uses an iterative minimum residual algorithm to find u_* that preserves code stability. The minimization algorithm was particularly developed so as to implement law-of-the-wall formulations that are appropriate to the description of flows subject to an adverse pressure gradient. This very sophisticated procedure will be described in detail elsewhere.

The computations were performed with a very fine mesh with 13888 nodes (P1-isoP2), and we should point out to the reader that a mesh with 13888 nodes is considered to be extremely fine for finite element standards. The computational grid is shown in Fig. 8.

4.2 Numerical results

The predicted general flow patterns are shown in Fig. 9b–d together with the experimental data (Fig. 9a).

The location of flow detachment was best predicted by the model of Nakayama and Koyama (1984). Unfortunately, this same model overpredicted the position of flow re-attachment by 34%, as illustrated in Fig. 9d. The formulation of Cruz and Silva Freire (1998, 2002) overpredicts detachment and underpredicts reattachment, resulting in a separated region 13.5% shorter than the experimentally determined length (Fig. 9b). The results obtained through Mellor's formulation overpredicted both the detachment and the reattachment points, as shown in Fig. 9c. This yielded a separation region with length $x/H = 6.00$, a value very close to the experimental value, $x/H = 6.17$.

Under the present mesh conditions, the classical law-of-the-wall was shown to be incapable of promoting flow separation. Table 6 summarizes the main findings.

Mean velocity profiles obtained by the different law-of-the-wall formulations are presented in Fig. 10 for the reverse flow region.

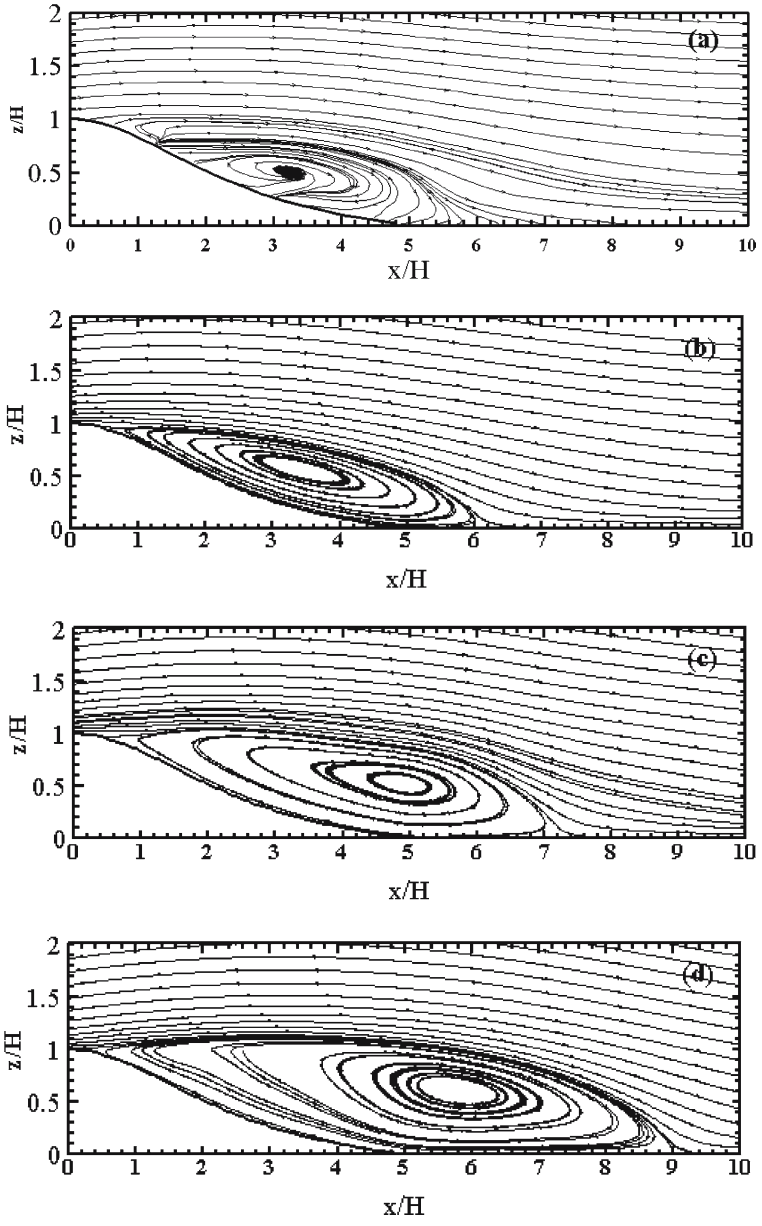

Fig. 9 Extension of bubble recirculation region according to (**a**) Experiments, (**b**) Cruz and Silva Freire (1998), (**c**) Mellor (1966) and (**d**) Nakayama and Koyama (1984)

The different mean velocity predictions for the different law-of-the-wall formulations are marked. The results provided by the classical law of the wall that completely failed in predicting the separation region are also shown in Fig. 10 for the sake of comparison. On the hilltop (Fig. 10a) all near-wall formulations underpredict the speed-up factor by an order of about 20%. The model of Cruz and Silva Freire (1998, 2002) furnishes slightly better results, but overall the agreement is not good. Close

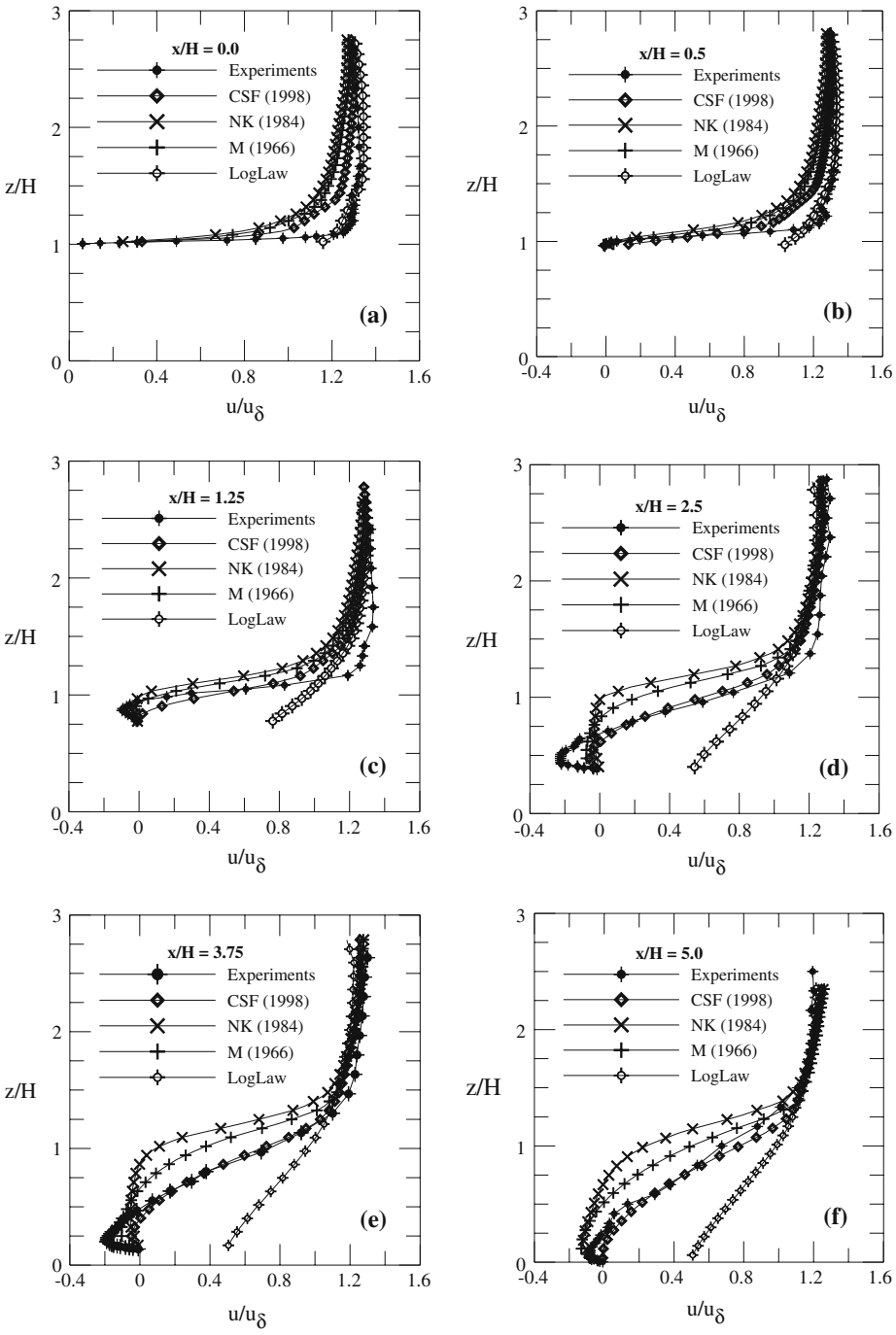

Fig. 10 Mean velocity profiles

Table 6 Length of separation bubbles according to different formulations

Formulation	Detachment (x/H)	Reattachment (x/H)	Length (L/H)
LogLaw	Not predicted	Not predicted	Not predicted
M (1966)	0.90	7.00	6.00
NK (1984)	0.60	8.90	8.30
CSF (1998)	0.80	6.10	5.30
Experiment	0.50	6.67	6.17

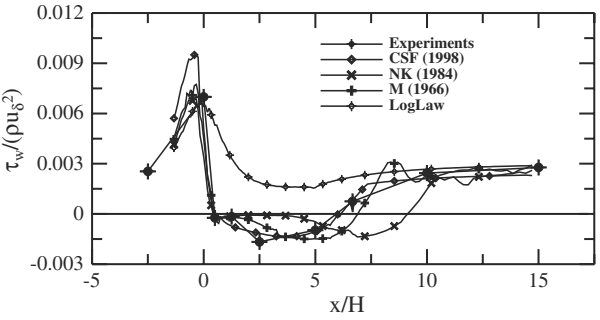

Fig. 11 Wall shear stress predictions, $\tau_w/(\rho u_\delta^2)$

to the separation point, at station $x/H = 0.5$, the differences between predicted and measured profiles are still large. In the reverse flow region (Fig. 10c–f), the very near-wall ($d/H < 0.2, d =$ distance from the wall) velocity behaviour appears to be captured only partially by the near-wall formulations. In fact, the agreement shown by all formulations at stations $x/H = 1.25$ and 5.0 is reasonable. However, at stations $x/H = 2.5$ and 3.75 the large peaks in reverse flow are not well predicted. Farther away from the wall ($d/H > 0.2$), across the remaining reverse flow region, the formulations of Mellor (1966) and of Nakayama and Koyama (1984) predict much lower velocities (Fig. 10d–f). However, the overall agreement provided by the formulation of Cruz and Silva Freire (1998, 2002) at station $x/H = 2.5$, 3.75 and 5.0 is very good.

To further investigate the near-wall behaviour of the proposed formulations, let us consider the wall shear-stress distribution. Here, we emphasize, predictions of wall shear stress were made directly from the near-wall formulations of Mellor (1966), of Nakayama and Koyama (1984) and of Cruz and Silva Freire (1998, 2002) as presented in Sect. 3. The results are shown in Fig. 11. On the hilltop, the inability of the formulations to resolve the near-wall layer furnishes an overestimation of τ_w. In the reverse flow region, however, the formulation of Nakayama and Koyama (1984) shows great fragility; the discrepancy from the experimental data is large. The predictions given by Mellor (1966) fail at stations $x/H = 1.25$ and 2.5, and at the other stations, agreement is poor. The formulation of Cruz and Silva Freire (1998, 2002) was observed to provide very good predictions of τ_w. The agreement at stations $x/H = 3.75$ and 5.0 was particularly good.

5 Final remarks

The present work reports new experimental data on the flow over a two-dimensional smooth steep hill. Mean and fluctuating quantities were measured through LDA for 13

different stations. In particular, the large separated region that was formed on the lee of the hill was characterized through seven different stations. The work characterized the mean velocity behaviour for both mean velocity components, showing in detail the near-wall reverse flow region. The data showed how turbulence production is largely enhanced in the separation region, yielding values of $\overline{u'^2}$, $\overline{w'^2}$ and $-\overline{u'w'}$ that are much higher than the values in the upstream undisturbed profile. Complementary plots illustrating other properties of turbulence, including the local turbulent kinetic energy, the production terms, the local mixing length and the local eddy viscosity will be presented elsewhere.

In addition, we have performed a numerical simulation of the flow via a finite elements code, Turbo-2D. The code models turbulence through a κ–ε model and uses wall functions to specify the boundary conditions. In the present numerical simulation, we have shown that predictions were very sensitive to the various types of near-wall formulations that were used. All three law-of-the-wall expressions that were specially devised to deal with adverse pressure gradients were capable of predicting the reverse flow region. However, the formulations of Mellor (1966) and of Nakayama and Koyama (1984) much underpredicted the flow velocity. The results of Mellor (1966) and of Nakayama and Koyama (1984) also gave poor predictions for the wall shear stress. Overall, the best mean velocity results in the reverse flow region ($X/H =$ 1.25, 2.5, 3.75 and 5.0) were given by the formulation of Cruz and Silva Freire (1998, 2002). This fact has been specially corroborated by the very good wall shear-stress predictions.

Acknowledgements The quality and legibility of this work has been greatly improved thanks to the many helpful comments and suggestions received from one referee. JBRL benefited from a Research Scholarship from the Brazilian Ministry of Education through CAPES. JBRL is also grateful to the Programme Alban, European Union Programme of High Level Scholarships for Latin America, identification number E03M23761BR, for the concession of further financial help regarding her stay at Oporto University. APSF is grateful to the Brazilian National Research Council (CNPq) for the award of a Research Fellowship (Grant No 304919/2003-9). The work was financially supported by CNPq through Grant No 472215/2003-5 and by the Rio de Janeiro Research Foundation (FAPERJ) through Grants E-26/171.198/2003 and E-26/152.368/2002. JLAFR and DVS are grateful to the Technology and Scientific Enterprise Foundation (FINATEC) from the University of Brasilia, for the material and financial support, which made the computational work possible. FTP is grateful to Prof. Maria Fernanda Proença and the Hydraulics Laboratory at Oporto University for all their help in setting up the flow rig and technical discussions.

References

Arya SPS, Capuano ME, Fagen LC (1987) Some fluid modelling studies of flow and dispersion over two-dimensional low hills. Atmos Environ 21:753–764

Athanassiadou M, Castro IP (2001) Neutral flow over a series of rough hills: a laboratory experiment. Boundary-Layer Meteorol 101:1–30

Brison JF, Buffat M, Jeandel D, Serres E (1985) Finite element simulation of turbulent flows using a two-equation model. In: Numerical methods in laminar and turbulent flow. Pineridge Press, Swansea, UK, pp 563–573

Britter RE, Hunt JCR, Richards KJ (1981) Air flow over a two-dimensional hill: studies of velocity speedup, roughness effects and turbulence. Quart J Roy Meteorol Soc 107:91–110

Brun G (1988) Development et application d'une méthode d'élement finis pour le calcul des écoulements turbulents fortement chaufées. Thèse de Doctorat, Ècole Centrale de Lyon, 156 pp

Buice C, Eaton J (1995) Experimental investigation of the flow through an asymmetric plane diffuser. Annual research briefs. Center of Turbulence Research, Stanford University, Nasa Ames, pp 117–120

Carlson JJ, Johnston JP, Sagi CJ (1967) Effects of wall shape on flow regimes and performance in straight two-dimensional diffusers. J Basic Eng 89 (March):151–160
Coles D (1956) The law of the wake in the turbulent boundary layer. J Fluid Mech 1:191–226
Cruz DOA, Silva Freire AP (1998) On single limits and the asymptotic behaviour of separating turbulent boundary layers. Int J Heat Mass Transfer 41:2097–2111
Cruz DOA, Silva Freire AP (2002) Note on a thermal law of the wall for separating and recirculating flows. Int J Heat Mass Transfer 45:1459–1465
Finnigan JJ (1983) A streamlined coordinate system for distorted turbulent shear flows. J Fluid Mech 130:241–258
Fontoura Rodrigues JLA (1990) Méthode de minimisation adaptée à la technique des éléments finis pour la simulation de écoulements turbulents avec conditions aux limites non linéaires de proche paroi. Thèse de Doctorat, Ècole Centrale de Lyon, 152 pp
Gong W, Ibbetson A (1986) A wind-tunnel study of turbulent flows over model hills. Boundary-Layer Meteorol 49:113-148
Grant ALM (1992) The structure of turbulence in the near-neutral atmospheric boundary-layer. J Atmos Sci 49:226–239
Hughes TJR, Brooks A (1979) A multi-dimensional upwind scheme with no crosswind diffusion. Finite element methods for convection dominated flows. ASME-AMD, New York 34:19–35
Kelly DW, Nakazawa S, Zienkiewcz S (1980) A note on upwinding and anisotropic balancing dissipation in finite element approximations to convective diffusion problems. Int J Numer Methods Eng 15(11):1705–1711
Khurshudyan LH, Snyder WH, Nekrasov IV (1981) Flow and dispersion of pollutants over two-dimensional hills. Env Prot Agency Rpt No EPA-600/4-81-067. Research Triangle Park, NC, 130 pp
Kim J, Kline SJ, Johnston JP (1980) Investigation of a reattaching turbulent shear layer: flow over a back-ward facing step. J Fluids Eng 102:302–308
Launder BE, Spalding DB (1974) The numerical computation of turbulent flows. Comput Meth Appl Mech 3:269–289
Mansour NN, Kim J, Moin P (1989) Near-wall kappa-epsilon turbulence modelling. AIAA J 27(8): 1068–1073.
Mellor GL (1966) The effects of pressure gradients on turbulent flow near a smooth wall. J Fluid Mech 24:255–274
Millikan CB (1939) A critical discussion of turbulent flow in channels and tubes. Proc. 5th Int. Cong. App. Mech. J. Wiley, New YorK, pp 386–392
Nakayama A, Koyama H (1984) A wall law for turbulent boundary layers in adverse pressure gradients. AIAA J 22:1386–1389
Prandtl L (1925) Über die ausgebildete Turbulenz. ZAMM 5:136–139
Reneau LR, Johnston JP, Kline SJ (1967) Performance and design of straight two dimensional diffusers. J Basic Eng 89 (March):141–150
Simpson RL, Chew YT, Schivaprasad BG (1981) The structure of a separating boundary layer. Part 1: mean flow and Reynolds stresses. J Fluid Mech 113:23–51
Stratford BS (1959) The prediction of separation of the turbulent boundary layer. J Fluid Mech 5:1–16
Trupp AC, Azad RS, Kassab SZ (1986) Near-wall velocity distributions within a straight conical diffuser. Exp Fluids 4:319–331